GNSS-Based Passive Airborne Radar: Hybrid-Aperture Sensing and Airborne Test Plans

Randy Silver, Hernan Suarez, Yan (Rockee) Zhang, Yih-Ru Huang and Mansur Tyler
Intelligent Aerospace Radar Team (IART)
University of Oklahoma,
Norman, OK 73072
rockee@ou.edu

1. Introduction

The past two decades has witnessed a renaissance in passive radar research. One of the areas of research in passive radar that has received recent attention is the use of reflected GNSS signals as the signal-of-opportunity for bistatic synthetic aperture radar (BSAR), known as space-surface BSAR (SS-BSAR) [1-7]. SS-BSAR is unique because it uses GNSS signals, which, in the case of the US owned and operated Global Positioning System (GPS), provide almost constant coverage to almost the entire earth [8-10]. Furthermore, the GPS satellites transmit left and right-hand circularly polarized signals combined during transmission to form a right-hand circularly polarized (RHCP) signal; the benefits being, when compared to horizontal or vertical polarized waveforms, is the signal reflection re-radiates in the opposite, or left-hand circularly polarized (LHCP), polarization with signal loss ranging from 15 to 20 dB [5, 10]. One major drawback to using GPS as the signal-of-opportunity is that the received signal level is extremely low, and lower when reflected (see Table 1) [2]

Table 1: L1-Band C/A Code Link Budget for a Linearly Polarized Antenna with 3-dB Gain

User minimum received power	-158.5 dBW (-128.5 dBm)
User linear antenna gain	3.0 dB
Free space propagation loss (FSPL)[1]	184.4 dB
Total atmospheric loss	0.5 dB
Polarization mismatch loss	3.4 dB
Required satellite EIRP[2]	26.8 dBW (56.8 dBm)
Satellite antenna gain at 14.3°, worst-case BLK II off-axis angle (dB)	13.4 dB
Required minimum satellite antenna input power	13.4 dBW (43.4 dBm or 21.9 W)

Furthermore, assuming an additive white Gaussian noise channel for simplicity:

$$P_N = kTB = 1.380 \times 10^{-23} \left(\frac{J}{K}\right) \times 300(K) \times 2\,MHz \qquad (1)$$
$$= -141\frac{dBW}{Hz} \left(or - 111\frac{dBm}{Hz}\right)$$

Thus, without processing, the SNR is approximately -37.5 dB for the reflected signal with the receiving antenna specified in Table 1.1. Even with a potential processing gain of approximately 46 dB calculated as:

$$G = \frac{BWpre}{BWpost} = \frac{2\,MHz}{50\,Hz} = 46\,dB, \qquad (2)$$

---

[1] FSPL is calculated as $L_{fs} = 10log_{10}[\frac{4\pi r^2}{\lambda^2}]$,

[2] Effective Isolated Radiated Power; defined (in dB) as EIRP = Power Transmitted + Gain of the Transmitter

the resulting SNR will still be low at 8.5 dB. Regardless of the potential challenges, the benefits of SS-BSAR (i.e. passive covert imaging for intelligence, surveillance, and recognizance (ISR) missions using UAVs, ground surveys in difficult terrain using UAVs, medical imaging, etc.) greatly outweigh the challenges.

Studies done in the UK [3-4, 6] have demonstrated the efficacy of SS-BSAR using GNSS–specifically, the European-designed and -controlled Galileo. However, the current solutions are not enough to convince the scientific community of its effectiveness and reliability. Current systems for GNSS based SS-BSAR use cylindrical horn or dish antenna for signal collection and use hardware-defined or software-defined receivers for signal processing [3-7]. These systems are lacking in their ability to:

1. Resolve low signal level issues, multipath interference – which degrades image quality
2. Manipulate and store received signals (if using hardware-defined systems)
3. Provide good phase coherency with reference receivers and data collection, and
4. Reduce cost, size, weight, and power (C-SWaP) for potential UAV use.

Work has been done to create software receivers with phase coherency and C-SWaP in mind [5]. Esterhuizen et al. presented the development of software designed to maintain phase coherency of the line-of-sight (LOS) reference channel and the reflected signal channel while constraining the receive hardware and computer for storage and processing to a single-board computer. Low-signal levels and multipath issues were not considered.

2.   Sensing Analysis and Simulation

Before delving into the physical design, construction, and testing of the GPS passive bistatic radar system, it is important to understand and explore the basic principles of receiving reflected GPS signals for imaging purposes. Thus, a discussion of the background and simulations is necessary to understand the feasibility of an implementing a phased array as a passive radar system. Therefore, it is crucial to the success of this project to have a basic, yet solid, understanding of GNSS as a radar signal-of-opportunity. We begin with an introduction to imaging scenarios with GNSS as a non-cooperative transmitter (NCT) for the passive bistatic radar. The following sections will introduce the GPS signal structure, satellite transmission, and passive radar reception. Next, a discourse of a software-defined receiver approach over a traditional hardware-defined receiver configuration is given. Continuing further, a discussion on the design of the array, as well as the selection of a uniform linear array, will be provided.

2.1 GNSS As Radar Signal of Opportunity

Global Navigation Satellite Systems (GNSSs) provide users with positioning information for a variety of different uses, such as military, synchronization, air-traffic control, etc. Three different GNSSs orbiting the earth are discussed in this paper: the U.S. Global Positioning System (GPS), the European Galileo positioning system – known as Galileo, and the Russian GLObal NAvitaion Satellite System (GLONASS). Each of these satellites orbit the earth at or very near the medium earth orbit (MEO), approximately 20,200 km from the earth's surface, resulting in an orbit time very close to 12 hours. Each scheme is designed to provide at least four "visible" satellites at any point on earth at all times to correctly calculate latitude, longitude, and estimated height above sea level by using known parameters of each satellite, which is transmitted to earth and collected by GNSS receivers for decoding and calculations. Figure 1 provides a general diagram of the positioning scheme employed by GNSS.
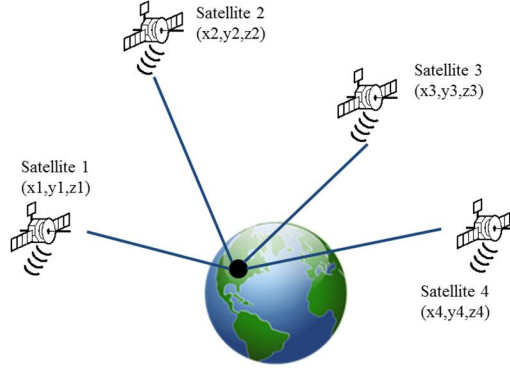
Figure 1: Example of GNSS positioning

2.2 Reliability and Availability

All satellite systems compared were considered to be reliable in the sense that they all orbit the earth in well understood fashions and reliably transmit information to the surface of the earth. However, they are not equal in terms of availability. GNSS has been proven to be the only system that provided not only global coverage, but also guaranteed the most satellite coverage for the longest amount of time. Thus, the chances of detecting a usable signal and applying its data are more likely with GNSS than other systems considered. Another benefit of deploying multiple satellites is the capability to survey the received satellites and select the satellite that provides the most opportune signal depending upon geometry and targets of interest. Drawbacks to using GNSS are limited bandwidth and relatively low signal power which are not ideal for radar applications, especially a passive radar that provides little to no gain of its own.

2.3 Resolution Consideration

Equation (3) provides the range resolution for a bistatic radar:

$$\delta_{rb} = \frac{\delta_{rm}}{\cos(\frac{\theta_b}{2})} \tag{3}$$

where δ_{rb} is the bistatic range resolution and θ_b is the bistatic angle – the angle between the transmitter line-of-sight (LOS) and the receiver LOS, illustrated in Figure 2. The variable δ_{rm} is the monostatic range resolution, defined as:

$$\delta_{rm} = \frac{c}{2B} \tag{4}$$

where c is the speed of light in a vacuum and B is the signal bandwidth.
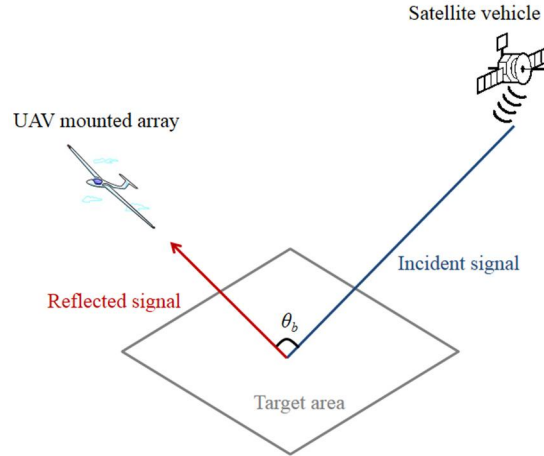
Figure 2: Simplified space-surface bistatic geometry illustrating the bistatic angle, θ_b

For the case of GPS, for example, the best-case range resolution for the L1-band C/A code is 150 meters, much less than can be expected for any of the other satellite systems compared. Fortunately, cross-range resolution, defined as equation (5):

$$\delta_{cr} \cong \frac{\lambda X_c}{4L\cos^2\theta_n(0)} \qquad (5)$$

,where λ is the signal wavelength, X_c is the distance of the target from the receiving antenna, L is the receiving antenna aperture length, and $\theta_n(0)$ is the main-lobe beamwidth of the receiving antenna, can be controlled by receiving antenna design. As an example, consider a target distance of 1000 meters at L1-band, with an aperture of 3 meters and a beamwidth of 5°. The resulting cross-range resolution is approximately 17 meters at boresight, which degrades as the beamwidth widens as it is steered off boresight to a beamwidth of approximately 20°, giving a cross-range resolution of approximately 27°, considering a change of target distance due to geometric change. Both of these values can be improved by using a narrower beamwidth and larger aperture. Thus, the conclusion can be made that the cross-range resolution is greatly improved by using a large receiving antenna with a narrow beamwidth while ensuring the targets are a sufficient distance away from the receiving antenna. Using two-dimensional imaging techniques can improve the overall target resolution and still places GNSS as a signal-of-opportunity as a viable solution.

2.4 Power Spectrums

Zuo [3] derives several calculations that demonstrate the received power spectral density (PSD) of the compared satellite systems, showing that GNSSs receive approximately 10 dB less power than their counterparts. However, more satellites provide the opportunity to choose the satellite that has the best geometry to provide the highest PSD, which is an advantage of GNSS. Also, GNSSs have many commercial receivers, both hardware- and software-based, that increase the signal-to-noise ratio of the received signal. Specific to software-based receivers, signal processing techniques such as beamforming and digital matched filtering, coupled with processing gains from demodulating the received signal, can provide SNR boosts of up to 40-50 dB. Furthermore, the relatively high volume of satellites improves the ground coverage of the GNSS signal, while also having as little as 2-dB power level change over an elevation range from 5° to 110° as is the case with GPS [2], allowing for an assumption of constant signal coverage over a large ground area, simplifying phase calculations as well as reducing transmitter-to-ground angular dependencies.

3. HYBRID-APERTURE IMAGING THEORY AND SIMULATIONS

Several challenges toward the use of GNSS were presented, and the technologies and designs described afterward attempt to provide carefully constructed solutions to the issues of gain and power-loss. Trying to strictly create images without decoding/processing the received GPS information would be nearly impossible, if only for the horrendous range resolution – 150 meters – that would result [see 3,12,14]. However, combining the passive array and the SDR, C/A coding and the navigation message can be removed from the signal, leaving only a tone that represents the topography of the illuminated area. Take, for instance, the following imaging scenario, shown as Figure 3.
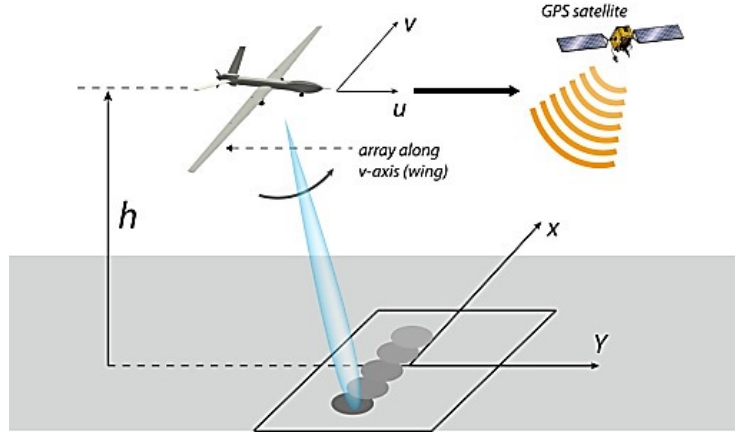
Figure 3: Example imaging scenario. The receiver flight path along the synthetic aperture while scanning the real-aperture. A LOS reference is affixed to the receiver and is used to compensate for Doppler shift phase error. The GPS satellite provides constant imaging area illumination.

As the receiver moves along the synthetic-aperture dimension, sweeping the real-aperture dimension, the reflected signal collected by the receiver is represented by:

$$s(u,v) = \sum_n s_n(u,v) = \sum_n \sigma_n e^{-jk\sqrt{h^2+(x_n-u)^2+(y-v)^2}} \tag{6}$$

where σ_n is the reflectivity of the nth target at a specific location defined as (x_n, y_n), k is the spatial frequency defined as $\frac{2\pi}{\lambda}$, u is defined as the direction of the synthetic-aperture, v is the direction of the real-aperture, and only the baseband portion of the received signal is shown. Equation (6) defines the two-dimensional array, to which can be applied the following beamforming method to "steer" the beam for imaging purposes:

$$\hat{e} = \frac{(x,y,0)}{\sqrt{x^2+y^2}} \tag{7}$$

Taking the inner product of equation (7) and the real- and synthetic-aperture position vector, (u,v,h), as follows:

$$d(u,v) = \hat{e} \cdot (u,v,h) = \frac{xu+yv}{\sqrt{x^2+y^2}} \tag{8}$$

which has a physical representation of the ground-to-receiver propagation path difference. Coherently summing the "steered" beam across the real- and synthetic-aperture dimensions produces the beamformed image, assuming that all of the path differences are represented in the reflected signal for a specific point (x,y). Mathematically, this is represented as:

$$S_b(x,y) = \sum_{u,v} s(u,v)e^{-jkd(u,v)} \tag{9}$$

Another method to reconstruct the image is to use a matched filter approach. F. Kong derives the Fourier transform of equation (9):

$$S(k_u, k_v) = e^{-jh\sqrt{k^2 - k_u^2 - k_v^2}} \sum_n \sigma_n I_n(k_u, k_v) e^{-j(x_n k_u + y_n k_v)} \qquad (10)$$

where k is the spatial frequency, k_u and k_v are the spatial frequency variables in the real- and synthetic-aperture domains. $I_n(k_u, k_v)$ defines the frequency domain support:

$$I_n(k_u, k_v) = \begin{cases} 1 & k_u \in \left[-k\frac{x_0 + L_u}{\sqrt{h^2 + (x_0 + L_u)^2}}, k\frac{x_0 + L_u}{\sqrt{h^2 + (x_0 + L_u)^2}} \right], \\ & k_v \in \left[-k\frac{y_0 + L_v}{\sqrt{h^2 + (y_0 + L_v)^2}}, k\frac{y_0 + L_v}{\sqrt{h^2 + (y_0 + L_v)^2}} \right] \\ 0 & otherwise \end{cases} \qquad (11)$$

The reference signal is constructed as:

$$s_0(u, v) = e^{-jk\sqrt{h^2 + u^2 + v^2}} \qquad (12)$$

and its Fourier transform is:

$$S_0(k_u, k_v) = e^{-jh\sqrt{k^2 - k_u^2 - k_v^2}} \qquad (13)$$

where h is the height above the ground. The matched filter then becomes:

$$S_M(k_u, k_v) = S(k_u, k_v) S_0^*(k_u, k_v) \qquad (14)$$

and directly mapping (k_u, k_v) to (k_x, k_y), the resulting equation represents the reconstructed image in the spatial frequency domain:

$$S_M(k_x, k_y) = \sum_n \sigma_n I_n(k_x, k_y) e^{-j(x_n k_x + y_n k_y)} \qquad (15)$$

Taking the inverse Fourier transform, the reconstructed image becomes:

$$s_m(x, y) = \sum_n \sigma_n i_n(x - x_n, y - y_n) \qquad (16)$$

where $i_n(x, y)$ is the point-spread function, which defines the radar response of an ideal point function and which time-domain expression defines the radar range resolution.

The simulation in Figure 4 demonstrates the scenario of a UAV borne linear array of 21 half-wavelength spaced antenna elements, encompassing 1.9 meters, capturing data for 9.5 meters, creating a synthetic array of 101 elements × 21 elements, at a height above ground level of 50 meters.

Reconstructed image by matched filter
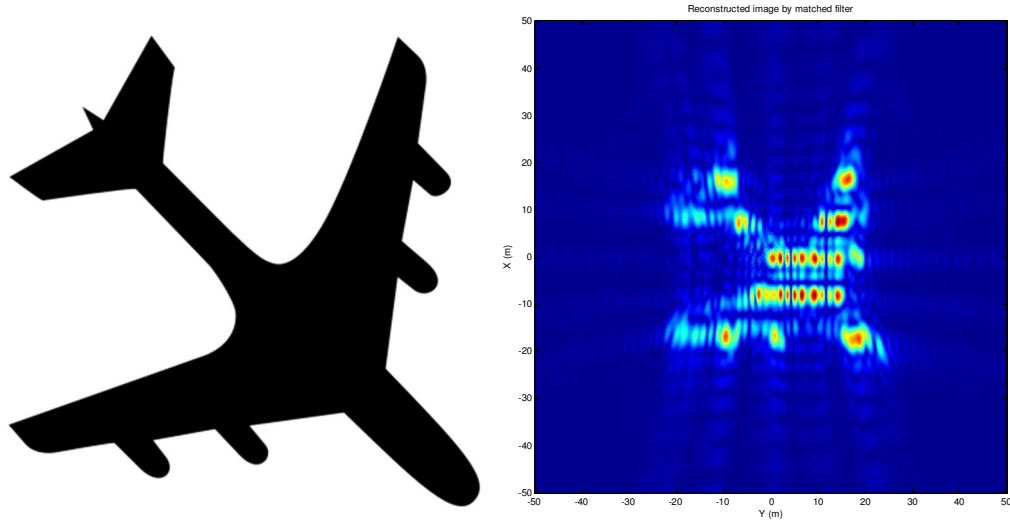
Figure 4: Example simulation results.

4. Prototype Instrumentations

The GPS array system consists of two smaller subsystems: The GPS antenna array and the GPS software-defined radar receiver (SDRR). These two subsystems are connected by the analog beamformer (ABF) system via ribbon cable. The subsystems, including the individual components that compose each subsystem, are fully defined and described in the following sections of this chapter. Figure 5 provides a high-level view of the GPS passive bistatic radar system.
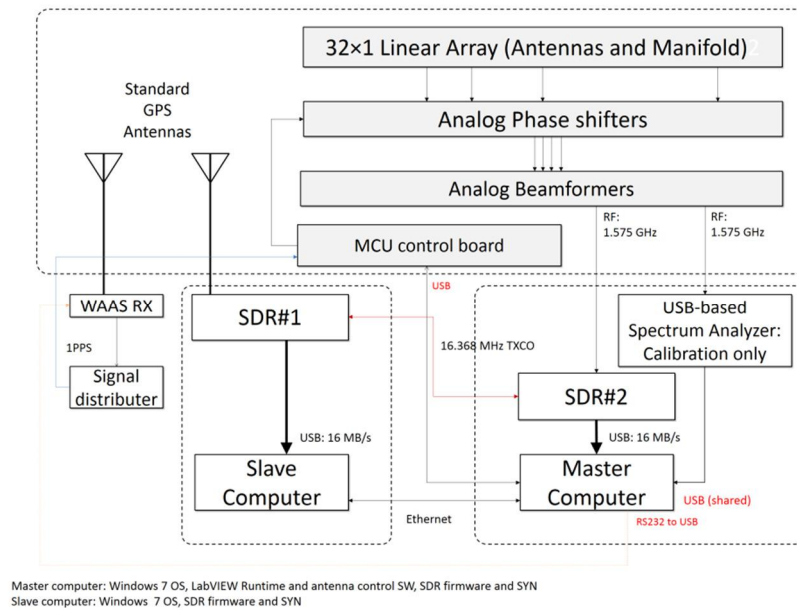

Figure 5: GPS passive bistatic radar overall high-level system diagram

The GPS antenna array subsystem consists of the following components:

-Aluminum U-channel for mounting the components of the subsystem
-32 left hand circularly polarized, pin-fed microstrip patch antenna elements
-Analog phase- shifter printed circuit board (PCB), which is part of the analog beamformer (ABF) subsystem and controlled by the ABF control PCB (described in section 3.2)
-4, 9-to-1 power combiners with one port terminated with a 50-ohm load
-1, 4-to-1 power combiner

The received signals gathered by the antenna elements are routed to the ABF phase-shifter PCB subsystem that is mounted on the opposite side of the aluminum U-channel, demonstrated by Figure 6. The 32 outputs from the antenna elements are carried by coaxial transmission lines and connected to the 32 signal inputs of the PCB. The 32 signals are phase-shifted by 32 individual Hittite analog phase-shifters, which are controlled by the ABF control PCB and connected via a ribbon cable that provides the analog control voltages that determines the phase-shift value.
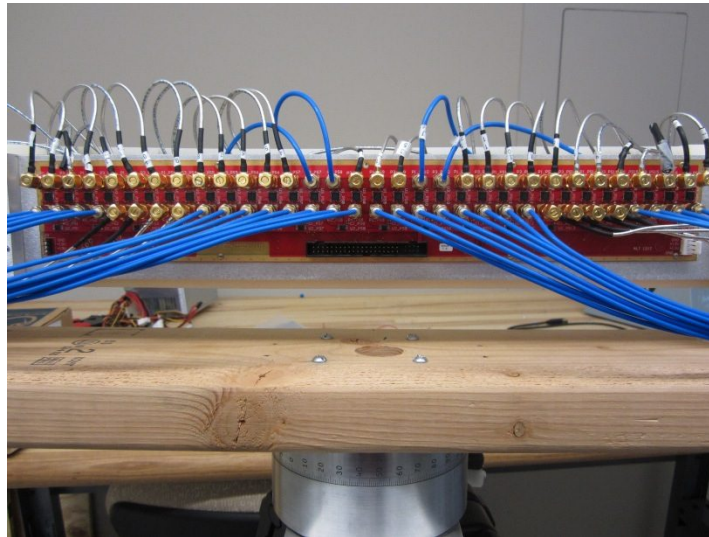
Figure 6: ABF phase-shifter PCB, showing the 32 input signals, 32 Hittite analog phase-shifters, and 32 output signals – which go the power combiners (ribbon cable connection to the ABF control PCB not shown)

The phase-shifted signals are routed to power combiners to complete the beamforming process. The ABF phase-shifter uses a 12V power input generated by the ABF control PCB to power the op-amp unity gain buffers, which provide stable reference voltage levels for the analog phase-shifters. Altium Designer was used to design the PCB and produce the Gerber files. The PCB was manufactured and an off-site PCB manufacturer applied the op-amps and Hittite analog phase-shifters to the PCB, while the SMA and power connectors were applied at the Radar Innovations Lab (RIL).

5. HYBRID-APERTURE EXPERIMENTS

5.1 Experiment Setup

On 6 May 2013, members of the RIL at the University of Oklahoma conducted a ground test with the GPS passive bistatic radar to create a 2-dimensional image. Two scans were taken between 16:55:30 UTC and 17:54:39 UTC (11:55:30 AM CDT and 12:54:39 PM CDT) on top of the National Weather Center in Norman, Oklahoma (hereafter denoted as NWC). The GPS antenna array is mounted on a custom-made aluminum rack approximately 6.5 feet tall and 2 feet wide (2 m tall by 0.6 m wide). In order to create a synthetic aperture, holes large enough for bolts to pass through were drilled into the aluminum rack, with 13 positions at half wavelength spacing (9.5 cm) creating a potential 2-dimensional array size of 32×13. To limit multi-path interferences and create more separation between synthetic-aperture scans, a copper "horn" aperture was added to the GPS antenna array around the center antenna elements. This copper "horn" aperture narrows the vertical beamwidth to approximately 30° from an estimated 180° vertical beamwidth and is shown in Figure 7.

The aluminum rack rests on a small stepper rotor that rotates the rack a possible 360 degrees in azimuth at a minimum speed of 1 degree per second. The rack and rotor are mounted on a 2 feet by 2 feet (0.6 m by 0.6 m) moving platform, which greatly eases transport of the GPS antenna array and rack-mount. The necessary electronics and data acquisition – less the rotor control – are contained in a metal box and are located near the GPS antenna array during data acquisition.

Two scans were taken from the roof of the NWC, facing north and targeting the SRC, located at 101 David L. Boren Blvd, Norman, Oklahoma. Test 1 began after 16:55 UTC and ended before 17:32 UTC and Test 2 began after 17:32 UTC and ended before 17:54 UTC. Each test took approximately 20 minutes to run, which consists of a 60 second physical rotation of the GPS antenna array (manual beamsteering), 60 seconds to reset the array, and 30 seconds to manually reposition the GPS Array. The extra time not accounted for by scanning and movement is due to the Wide Area Augmentation System (WAAS) reference receiver test, which occurred before Test 1, between Test 1 and Test 2, and after Test 2. Both tests scanned an area of approximately 63° clockwise in the real-aperture dimension (at approximately 1°/sec) with SRC located from -20° to +5° of the scan. The synthetic-aperture dimension is defined as elevation bins and corresponds to the physical elevation of the GPS antenna array. Refer to Figure 7 for the imaging area as seen from the roof of the NWC at OU and to Figure 8 for a sky-view of the imaging area. Refer to Figure 9 to view the testing setup.

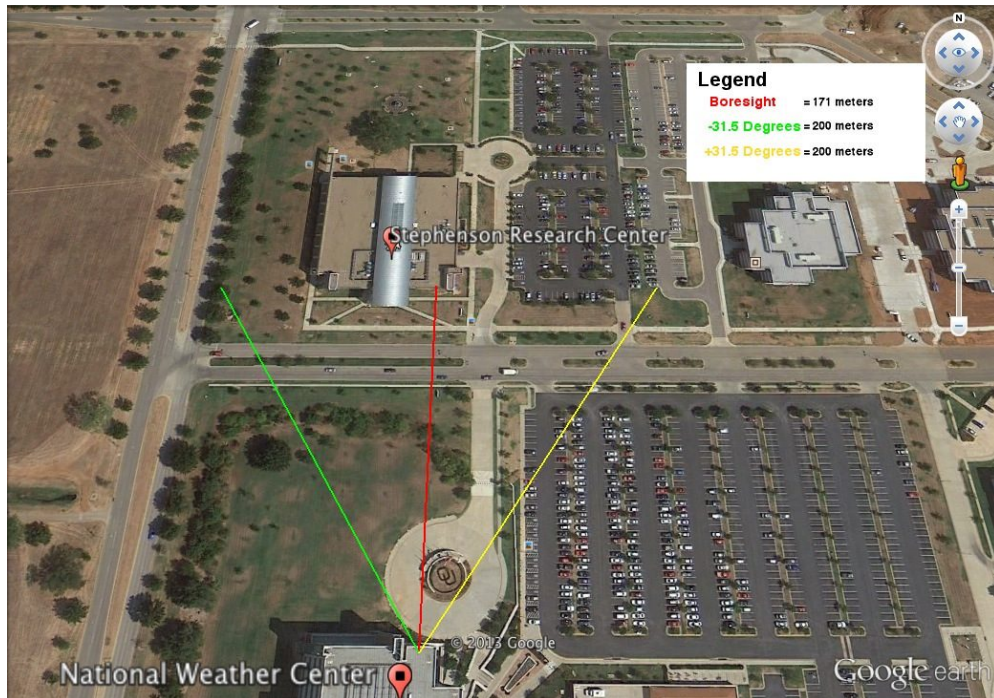**Figure 7: Imaging area for Test 1 and Test 2 from 6 May 2013**

Figure 8: Google Earth markup showing the imaging area for the ground tests from 6 May 2013


Figure 9: Hybrid-aperture testing setup on the northern part of the roof of the NWC at OU from 6 May 2013

5.2 GNSS Signal Processing

1. **Data Formatting**: Both array and reference receiver channel data are collected from the GPS SDRR. To begin formatting the data for post-processing, point the script to read the data at the start of the binary file. Then put the data into complex format ($I + jQ$) and begin parsing the data for the specified satellite vehicle (SV) as "acquired" by the WAAS reference receiver.
2. **Acquisition:** When a SV is successfully recognized, pass the data to the MATLAB program.
3. **Pre-Run Processing**: This portion of the program is important for the overall GPS functioning of the software-defined receiver (SDR) as it eliminates SVs that are not found and passes information in a condensed format, based upon the number of SVs one wishes to process (maximum of 6), to the next portion of the program.
4. **Demodulation:** The data is shifted to "baseband" – the Doppler shift is removed – and processed in 1 millisecond chunks, and then averaged over that 1 millisecond. The output of the data is given in 1 millisecond intervals for the duration of the data (e.g. if 63 seconds worth of data is recorded, the user has access to 63000 values to process; this step is necessary to successfully process the data on a standard computer as a dataset that is not averaged would be too large. This step does not hurt the GPS solution and does not appear to alter our image.) The program passes many variables to the user for the GPS portion of the code that we do not use. Therefore, for our purposes, we retain the I and Q "baseband" data for the next steps.
5. **Correlation:** The array and reference data (in complex $I + jQ$ form) are individually transformed to the frequency domain by a FFT – along the real-aperture domain for the array data – and multiplied together, thereby correlating the data. The combination is then multiplied with a low-pass, Kaiser filter in the frequency domain. The data are transformed back to the time domain by an inverse FFT along the real-aperture domain and then rearranged to the proper imaging order (by performing a matrix flip), then min/max normalized.
6. **Spatial Processing:** The array data is transformed to the frequency domain by an FFT along the synthetic-aperture dimension and sampled 256 times (64 times more than its standard 8) for spatial processing with a function representative of the synthetic-array beam shape – in our case, represented as a narrow Sinc function. The synthetic aperture data, in the frequency domain, is multiplied by an FFT of the abovementioned Sinc function, which creates a new array of spatial processed synthetic-aperture data. The matched filtered data is transformed to the time domain by an inverse FFT along the synthetic-aperture dimension, where the resulting data represents the reconstructed image. The first steps of the algorithm remove C/A modulation from the satellite, separation of I/Q data, and rudimentary Doppler shift removal. The two data sets are correlated together in the cross-range domain, after which the combined data is filtered and normalized. Finally, the data is processed with a matched filter in the range domain, resulting in the reconstructed image with the time-series data.

Figure 10 provides a high-level block diagram of the post-processing steps, providing an image of the major steps involved of demodulating the data, shifting if to baseband, removing the navigation message while synchronizing the data (the correlation step), and then performing the spatial filtering to create the reconstructed image.
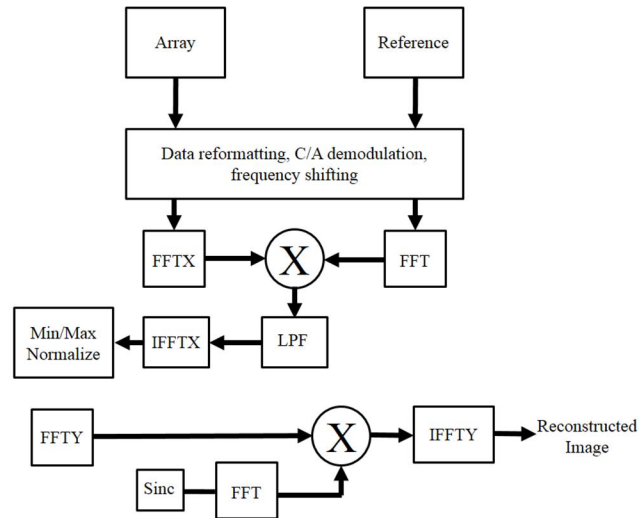
Figure 10: Post-processing block diagram. Transforms appended with "-X" occur along the real-aperture domain; whereas transforms appended with "-Y" occur along the synthetic-aperture domain

5.3 Initial Experiment Results

Shown below in Figure 11 is an image obtained from SV 32 using the data processing scheme from the previous section.
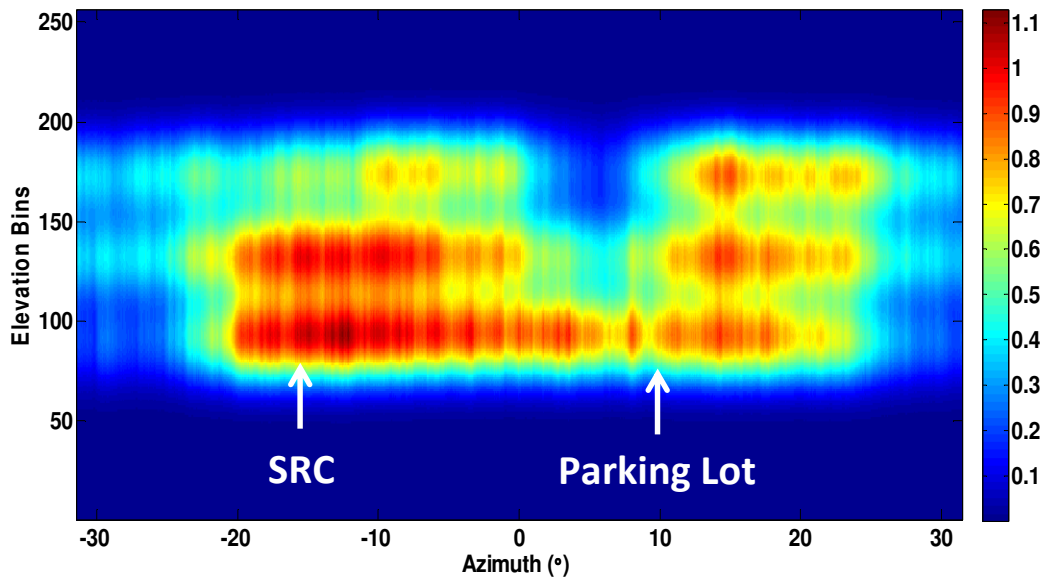

Figure 11: Test 1, SV 32: noncoherent spatial filtering from 6 May 2013; note the clear distinction of the SRC and the parking lot located due east

In Figure 11, which is the scan, clearly shows the SRC target identified from approximately -20° to +5°. You can also clearly see a very high reflectivity portion from +10° to +25°, which is the parking lot due east of the SRC.

As noted in [16], the images produced from the scanning are very dependent on SV geometry. Refer to Figure 12 for a sky chart of the SVs from Test 1 and Test 2, respectively, used for the images produced.
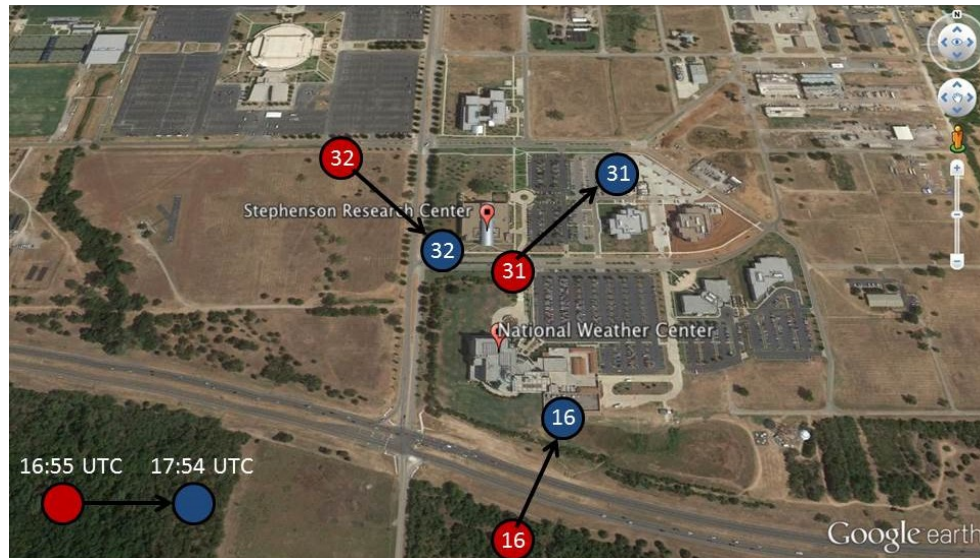
Figure 12: Relative position and movement of SVs 16, 31, and 32 from 16:55 UTC to 17:45 UTC on 6 May 2013

Note that the positions of the SVs are very different for two cases. Therefore it is expected that the illumination area for each SV will be slightly different. Furthermore, the data received at our GPS antenna array will greatly depend on the re-radiation of the SV transmitted energy from the targets in our imaging area. For example, SV 16's energy will propagate toward the SRC and then primarily backscatter toward our GPS antenna array. Whereas SV 32's energy, coming from higher in the sky and more toward the east, will reflect from the SRC in a different manner, which may represent a stronger or weaker reflection coefficient depending on the target's bistatic radar cross-section, which is determined largely by SV to target to GPS antenna array geometry. Also notice the imaging results from SV 32 from Test 2, shown as below as Figure 13.
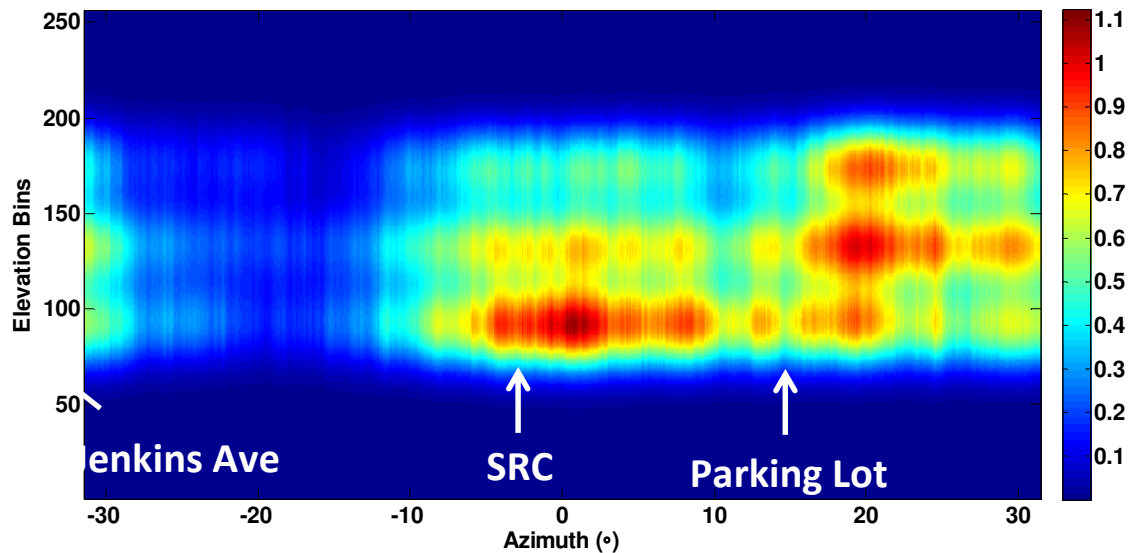
Figure 13: Test 2, SV 32: noncoherent spatial filtering from 6 May 2013; note the difference from Figure 16 in the position of the targets – SRC and the parking lot – and the inability to distinguish the two targets.

There is significant difference in target signatures between Test 1 and Test 2. However, neither image is wrong *per se*. Again, refer to the locations of SV 32 in Test 1 and Test 2. Notice that the satellite illumination locations between tests is very different, with almost 30° movement in azimuth and about 10° change in elevation. Referring to [2], satellite power change is roughly 2 dB change over 100° change in elevation, which is minimal. However, the combined effect of changing elevation and azimuth significantly alters the scattering characteristics of the targeting environment. Therefore, as noted in the differences between images for SV 32 in Test 1 and Test 2, the images will look different. Interestingly, some portions of the images experienced little effect from SV geometry, e.g. the parking lot in the portion of the images from +10° to 31.5°, which appears to have an almost uniform bistatic scattering signatures.

References

[1] K. Borre, D. M. Akos, N. Bertelsen, P. Rinder, S. H. Jensen, *A Software-Defined GPS and Galileo Receiver: A Single-Frequency Approach*, Birkhäuser, Boston, MA, 2007
[2] E. D. Kaplan, C. J. Hagerty, *Understanding GPS, Principles and Applications*, 2nd Edition, Artech House, Boston, MA, 2006, pp. 113-151
[3] R. Zuo, "Bistatic Synthetic Aperture Radar Using GNSS as Transmitters of Opportunity," Doctoral Dissertation, The University of Birmingham, England, UK, September, 2011
[4] M. Cherniakov, et al., *Bistatic Radar: Emerging Technology*, John Wiley & Sons, Ltd., England, UK, 2008, pp. 339-361
[5] S. Esterhuizen, "The Design, Construction, and Testing of a Modular GPS Bistatic Radar Software Receiver for Small Platforms," Master's Thesis, University of Colorado, 2006
[6] X. He, M. Cherniakov, T. Zeng, "Signal Detectability in SS-BSAR with GNSS Non-Cooperative Transmitter," *IEE Proceedings Radar Sonar Navigation*, Vol. 152, No. 3, June, 2005, pp. 124-132
[7] I. Walterscheid, T. Espeter, A. R. Brenner, J. Klare, J. H. G. Ender, H. Nies, R. Wang, O. Loffeld, "Bistatic SAR Experiments with PAMIR and TerraSAR-X – Setup, Processing, and Image Results," *IEEE Transactions on Geoscience and Remote Sensing*, Vol. 48, No. 8, August, 2010, pp. 3268-3279
[8] U.S. Department of Defense, "Global Positioning System Standard Positioning Service Performance Standard," 4th Edition, September, 2008

[9] Navstar GPS Space Segment/Navigation User Segment Interfaces, "Global Positioning System Directorate Systems Engineering & Integration Interface Specification IS-GPS-200," Rev. F, September, 2011

[10] F. M. Czopek, Lt. S. Schollenberger, "Description and Performance of the GPS Block I and II L-Band Antenna and Link Budget", *Proceedings of the 6th International Technical Meeting of the Satellite Division of the Institute of Navigation (ION GPS 1993)*, Salt Lake City, UT, September 22-24, 1993, pp. 37-43

[11] D. M. Akos, "A Software Radio Approach to Global Navigation Satellite System Receiver Design," Doctoral Dissertation, Ohio University, August, 1997

[12] F. Kong, "Passive and Bistatic Radar Imaging with Synthetic Antenna Apertures," General Exam Report, University of Oklahoma, March, 2011

[13] R. J. Doviak and S. S. Zrnić, *Doppler Radar and Weather Observations*, 2nd Edition, Dover Publications, Inc., NY, 1993, pp. 30-35

[14] M. Soumekh, *Synthetic Aperture Radar Signal Processing with MATLAB Algorithms*, John Wiley & Sons, England, UK, 1999, pp. 262-372

[15] U.S. Department of Transportation, "U.S. Department of Transportation Federal Aviation Administration Specification for the Wide Area Augmentation System (WAAS)", Change 2, August, 2001

[16] R. Silver, Y. Zhang, H. Suarez, Y. Pan, Y.-R. Huang, "GNSS-Based Passive Radar Sensing Using Hybrid-Aperture System", *Proc. SPIE* 8714, Radar Sensor Technology XVII, 871409, May, 2013, http://dx.doi.org/10.1117/12.2015421

[17] B. D. Van Veen and K. M. Buckley, "Beamforming: A Versatile Approach to Spatial Filtering," *IEEE ASSP Magazine*, April, 1988, pp. 4-24

[18] M. Skolnik, *Radar Handbook*, 3rd Edition, McGraw Hill, NY, 2008

[19] W. L. Stutzman and G. A. Thiele, *Antenna Theory and Design*, 2nd Edition, John Wiley & Sons, Inc., England, UK, 1998, pp. 56-142

[20] H. J. Visser, *Array and Phased Array Antenna Basics*, John Wiley & Sons, Ltd., England, UK, 2005

[21] R. J. Mailloux, *Phased Array Antenna Handbook*, 2nd Edition, Artech House, Boston, MA, 2005